Applied Ocean Research 161 (2025) 104636

Contents lists available at ScienceDirect

Applied Ocean Research

journal homepage: www.elsevier.com/locate/apor

Invited paper

Remote River Energy System: Field trial experiments in a tidal estuary

Ian Masters *, Ali Esmaeili, Iestyn Evans, Deepak George, David Glasby, Jose Horrillo-Caraballo, Thomas Lake, Dawn Morgan, Michael Togneri, Alison J. Williams

Zienkiewicz Institute for Modelling, Data and AI, Swansea University, Swansea, UK

ARTICLE INFO

Dataset link: Remote River Energy System (RRES) Field Trial - Full Scale device at Warrior Way, Marine Energy Test Area (META) - 01/2024 to 02/2024 (Original data)

Keywords:
Tidal Energy
Tidal turbine
Hydrokinetic
River current
Sustainable energy
Water pump
Renewable energy
Open source

ABSTRACT

A micro-grid renewable energy system with multiple types of generation is more reliable than a single source of supply. Underutilised potential sources of energy include rivers and tidal estuaries. Here we show field trial results from an open source river turbine suitable for power generation in remote locations worldwide.

This was the first tidal energy test carried out at the new Marine Energy Test Area in Pembrokeshire, Wales, UK, achieving Technology Readiness Level 5. The turbine and mechanical water pump power take off design were previously published, describing a low cost design that could be used for electrical generation or for direct use as a water pump. Further development of the design to provide additional measurement capability and improved utility as a research and test platform is described here, along with summaries of the design process, structured test programme and costs incurred during the process.

Operational and environmental data was successfully collected for both laboratory and field tests. The results show that the device was capable of operating in real world flow conditions at or slightly below its design optimum tip speed ratio but conditions on site did not permit testing up to the full design rating of the turbine. Some sensors failed to function or failed to function reliably, and the limitations this places on analysis of these results is highlighted. CAD drawings, other design documents and field data collected are available under an open-source licence to facilitate others to use the design presented here.

1. Introduction

There is now an established industry which is capable of generating energy from flowing water in rivers and tidal estuaries. Utility scale grid connected tidal energy converters have reached technical maturity and several 'first commercial' arrays are starting to be built and deployed, with projects such as the Shetland Tidal Array and MeyGen grid connected and generating for several years. The MeyGen project in the Pentland Firth delivered 10 GWh to the UK electricity grid during 2024 from an array of four 1.5 MW turbines (Grattan et al., 2024), and several other developers continue to test electricity generating tidal devices around the UK. Community scale turbines have also made progress, with a number of technologies available. This work is a contribution to the technology development of small scale turbines and follows on from a published design study (Masters et al., 2022).

The original design study noted that high costs remained a barrier to deployment of tidal turbines and that many existing designs were suited for faster flow areas as described in Kirke (2019), and that clean and affordable energy for all is part of the UN Sustainable Development Goals (United Nations, 2015). Most existing designs for tidal energy devices operate at higher flow speeds and are designed for aggressive tidal channels (Coles et al., 2021), but there is significant resource available at lower flow speeds that has not been economically viable to capture with current technology (Lewis et al., 2021). A device able to operate in lower speed tidal flows could allow this resource to be used to provide options (or additional options) for clean and affordable energy in more locations. For example, Bhui et al. (2025) highlights the potential for small scale turbines in the Ganges Delta.

1.1. Experimental hypothesis

Following this design requirement led to the turbine and platform design presented in Masters et al. (2022) – referred to as a "Remote River Energy System" (RRES) – which were designed to be reliable and with minimal requirement for specialised tooling or facilities during production, use, or maintenance of the device. To respond to that challenge the system was deliberately designed as a mechanical system without any electrical or sensing components required within the offshore part of the system. A mechanical water pump provided one

* Corresponding author.
E-mail address: i.masters@swansea.ac.uk (I. Masters).

https://doi.org/10.1016/j.apor.2025.104636
Received 18 December 2024; Received in revised form 12 May 2025; Accepted 26 May 2025
Available online 16 June 2025

practical solution to that challenge, but the low rotation rate expected of a tidal turbine in low flows would not be sufficient to operate a traditional impeller type water pump. This lead to the design of a positive displacement pump with direct mechanical connection to the river turbine, controlled by back pressure in the outlet pipe, with wet running main bearings and no requirement for mechanical seals.

As part of the work described here, the system has been further developed to allow a prototype to be manufactured, deployed at a suitable location and tested. The opportunity was taken to measure the performance of the turbine and platform alongside the environmental conditions at the test site as part of this process. This meant that the test system used here is significantly more complex than the original concept in order to support the additional equipment, but the additional measurements provide more information about the site and the performance of the device. More specifically, the build and test of the prototype was focussed on the following key points:

1. To show that water pumping is a technically viable power take off solution at small scale, below the power and rotational speed range of widely available electrical machines.
2. To show that a standard blade design, coupled with wet running bearings, has good cut in speed and energy generation potential in low flows.
3. To prove local supply chains and low cost operations are possible for operation of a community scale river turbine
4. To collect multiple measurements of tidal flow data within a small proximity of each other, for future analysis.

The system was tested at the Marine Energy Test Area (META), which is a series of test sites in and around Milford Haven and the Pembrokeshire coast in south west Wales, UK. META consists of 8 sites, 5 of which are quayside sites for small scale testing and three are open water sites suitable for larger wave and tidal devices (Neill et al., 2023). The depth averaged flow speed at the site peaks around 1.4 ms^{-1} (Neill et al., 2023), which is greater than many river sites but still lower than the rated speed of many existing devices as shown in Fig. 2 of Lewis et al. (2021). This flow speed allows the RRES system to demonstrate operation and energy extraction in lower flows than areas which have been considered commercially to date. The costs involved with this test will also be discussed, but the emphasis of the tests carried out as part of this work was on demonstration of the device and measurement of its performance to inform future designs and deployments.

1.2. Site description

The site used for testing of the RRES system was the Warrior Way site, located upstream of the Cleddau Bridge and Pembroke Dock. The river upstream runs from the north east, curving around as it meets the minor tributary of Cosheston Pill before heading north west towards the bridge. This seabed within the site ranges from 9 m to 22 m below the mean sea level, with the deeper area of site situated in a distinct channel adjacent to a very steep shoreline. The majority of the site is flatter, but slopes away from the inside of the river bend. The RRES system was tested at the north western end of site with a mean water depth of 19 m, with a peak tidal range during testing of 5 m. Previous surveys and tests at the Warrior Way site shows similar ranges, with some variation depending on placement within the site (Neill et al., 2023; Lake et al., 2024).

2. Device design

The overall concept for the device remains as presented in Masters et al. (2022). The following sections describe how this concept was realised for the conditions at Warrior Way and how the additional instrumentation was incorporated.

Table 1
Detail of the cases used for the design of the RRES.

Case	Detail
1. Rated speed	1.3 ms^{-1} inflow at optimum TSR of 4.5 Used to determine the rated performance of the rotor
2. Peak power before shutdown	1.8 ms^{-1} inflow speed (shutdown limit), with TSR set at optimum to determine the maximum power before shutdown
3. Shutdown: Rotor parked	Rotor at 0 RPM, with a hypothetical 3.0 ms^{-1} inflow representing storm conditions. Thrust is based on plan area rather than swept area as blades are stationary
4. Runaway	3.0 ms^{-1} inflow and zero torque — represents mechanical failure with rotor spinning freely in worst case flow. This case will represent the highest thrust and rotational speed of the rotor blades
5. Peak torque before shutdown	As per case 2, but at a TSR providing peak torque. Used for specification of the bench rig motor
6. Startup torque	Torque required to start rotation. Targeted so that torque at 1.0 ms^{-1} > total frictional torque of RRES drive-train

2.1. Design load cases

Six different design cases were considered (see Table 1), each representing extremes of different conditions that could arise while operating at the META test site. These cases were then used to calculate loads acting on the rotor using blade element momentum theory (BEMT) (Togneri et al., 2020). Table 2 summarises the most important rotor loads and performance results for each design case.

2.2. Blade design

The rotor is made of two blades, each 1.2 m long, mounted to a central hub which is discussed further below. Each of the blades are made of glass fibre reinforced composite material, with an internal web and steel box section welded to a mounting plate as shown in Fig. 1. The NACA 63(3)-418 profile was used for the foil geometry, with the chord, twist and thickness along the length of the blade derived from the generic IFREMER geometry (Mycek et al., 2014).

For structural integrity, the blade geometry was modelled and analysed in SolidWorks. Finite element analysis was carried out using composite shell elements to represent the geometry and with the applied loads based on the design cases outlined in Tables 1 and 2. A mesh convergence study as shown in Fig. 3 was conducted to establish the optimum mesh size, with the resultant mesh shown in Fig. 2(a) and results shown in Figs. 2(b), 2(c), and 2(d). Fig. 2(b) shows the deflected shape of the blade structure, reporting a maximum of 11.6 mm deflection at the blade tip. Fig. 2(c) illustrates the von Mises stress distribution and shows the increased stresses around the termination of the steel box section. The resulting factor of safety diagram corresponding to Tsai–Wu failure criteria is shown in Fig. 2(d).

These results show the design is suitable; the section of blade close to the root experiences high bending moments and needs large sections compared to the tip region. The steel box section has a total length of 270 mm bonded to the web within the blade as shown in Fig. 1a and an increased number of layers used in the layup of the first 316 mm of the blade (as measured from the root/hub end) — 8 layers of 0/90 stitched glass fibre being used for the skin in this region and 5 layers in the remainder, with 12 layers used for the entire length of the web structure. After discussion with the manufacturer, the steel to fibreglass bond is reinforced by the addition of two long bolts (not shown in the drawing). They run through the steel in the chord-wise direction and are embedded into the composite layers on both sides.

Table 2
Summary of key rotor loads and performance for all RRES design cases.

Case	Torque (kN m)	Power (kW)	Thrust (kN)	Rotational rate (Hz)	TSR	Tip velocity (m/s)	Flow velocity (m/s)
1	0.79	3.07	4.22	0.62	4.5	5.85	1.3
2	1.76	6.98	6.79	0.62	3.3	5.85	1.8
3	0.86	0	4.02	0	0	0	3.0
4	0	0	17.68	3.88	12.2	36.60	3.0
5	1.76	6.77	6.52	0.61	3.2	5.75	1.8
6	0.10	0	0.45	0	0	0	1.0

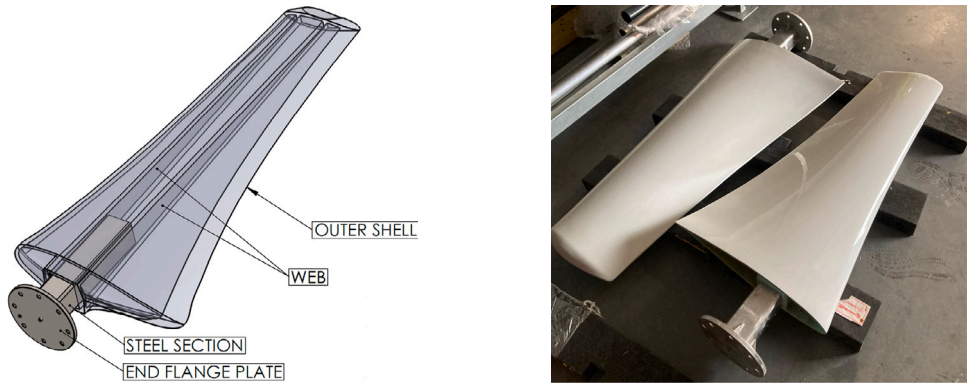

Fig. 1. (a) Design overview with components labelled (b) image of two blades, as manufactured.

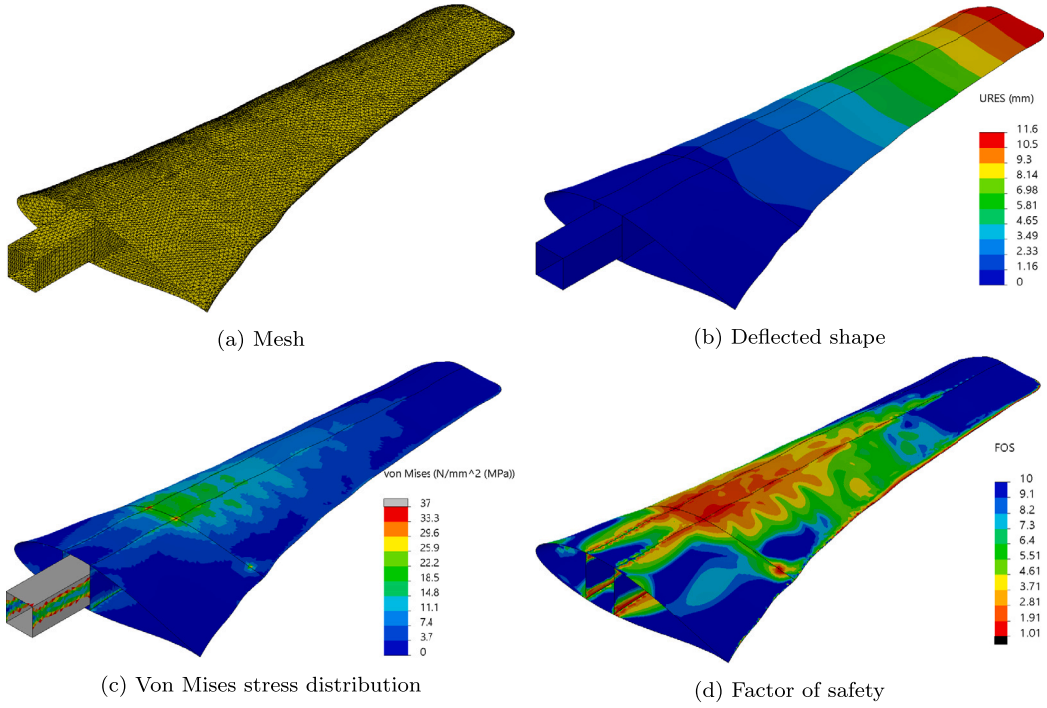

(a) Mesh (b) Deflected shape

(c) Von Mises stress distribution (d) Factor of safety

Fig. 2. FEM analysis results in SolidWorks.

2.3. Mechanical design

The mechanical design, developed from the existing design in Masters et al. (2022), was modified to incorporate the various sensors described in the sections below. The design was also modified to reduce the cost and lead time for prototype parts, in particular those used in the drivetrain and the pump, with commercial off the shelf components in many areas and laser cut plate material used where possible to limit the amount of custom fabricated parts required.

The mechanical design used for this test has been made available publicly as a 3D CAD model, including the mooring arrangements used at the Warrior Way site, on Zenodo (Masters et al., 2023).

2.3.1. Turbine design

The turbine uses two of the blades described above, mounted to a central hub providing an overall rotor diameter of 3 m. An overview of the blades and shaft assembly is given in Fig. 4.

The blades are fixed to the hub via an instrumented mounting adapter machined from stainless steel (shown in green on Fig. 4 and

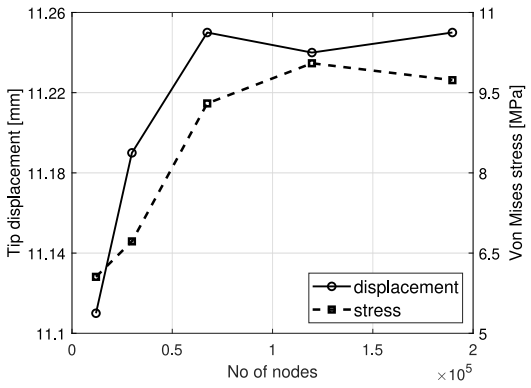

Fig. 3. Mesh convergence study.

discussed further in Section 3.2). The blade root uses slotted holes to allow it to be bolted to the mounting adapter regardless of the initial pitch angle selected, with a plate inserted between blade root and mounting adapter to allow the blade pitch angle to be set and maintained consistently. The flanged connection on the end of the blade has an alignment pin on its face which mates to holes in the thin metal plate, which has a second set of holes that mount to a corresponding pin on the mounting adapter. The holes in the plate are paired to allow repeatable selection of the blade pitch angle between 0 and 15 degrees.

The hub is welded to the first part of the shaft assembly which runs on bearings within a welded steel chassis "box". The flange connection between the root bending sensor and the hub is watertight to create a dry internal space inside the root bending sensor and hub for the strain gauges and wiring to be routed through the hub and into the driveshaft.

2.3.2. Driveshaft

The total driveshaft length is 1.4 m which gives space to accommodate the hub, thrust and journal bearings, torque sensor spacer, a sealed instrumentation capsule, and PTO connection. The driveshaft is bolted together from three individual parts: the hub, the torque sensor spacer, and the main shaft. This design allows an inline flange mounted torque sensor to be fitted, but this was not available for these tests. The driveshaft is partially hollow to allow the strain gauge wires to pass through to the sealed capsule on the main shaft. This arrangement was in part based on the work described in Allmark et al. (2020).

The capsule contains a slip ring, speed sensor, temperature and humidity sensor, and supporting electronics to transmit readings from these back to the control system. Mechanical seals are used in the capsule and between the adjoining sections of the driveshaft as shown in Fig. 4. The driveshaft diameter (75 mm) increases the linear speed of the shaft surface, which is necessary for proper functioning of the polymer bearings used. It also permits a cable to pass through to the hub to connect to the strain gauges, but as a consequence of these two criteria it is oversized for the mechanical loads expected. This results in a safety factor of 3.5 compared to the maximum predicted turbine torque.

2.3.3. Bearings and housing

In keeping with the original project design objectives in Masters et al. (2022), plain wet running bearings were chosen for the driveshaft as a low cost option that also removes the need for sealed rolling element bearings and (in principle) the need for regular maintenance of these components. The bearings are composite with a brass shell and the river water acts as the lubricating fluid. Fig. 4 shows in blue the locations of the two journal bearings and two thrust bearings on the driveshaft. The thrust bearings are made from brass and have a clearance gap to a stainless collar on the main shaft. They are also located behind the torque sensor spacer so that thrust measurements could theoretically be taken using a torque/thrust sensor. The driveshaft housing and bearing housings are fabricated from mild steel coated with marine grade paint. A sacrificial anode was fixed to the main housing to reduce corrosion on the housing.

2.3.4. Power Take-Off (PTO)

A single cylinder, dual acting piston pump converts turbine rotor power into water flow through a closed loop system. In the final design, the pressurised water flow could be used for irrigation or to run an onshore microhydro electricity generator. In the test setup, the pump pulls water from a freshwater supply (stored in an Intermediate Bulk Container (IBC) located on the barge deck) and pushes it through an inline throttle valve and a 1" orifice plate on the delivery line before discharging back into the tank. The throttle valve and orifice plate are used as a simple, low cost solution to imitate the generator in the system and create torque on the shaft for turbine control. This allows the novel parts of the design to be demonstrated without the additional cost and complexity of a generator and load bank.

A schematic of the PTO system is shown in Fig. 5. Although the RRES design intent is for pipelines to run to shore, for simplicity and ease of testing the tank and 'generator' were located on the barge deck. The pipework between the pump, throttle valve and the tank was reduced to a 2" diameter, adding pressure losses to the system in order to mimic pipe friction losses that would have been present in longer but larger diameter runs of pipework to shore. The pump crank mechanism mounts directly onto the rear end of the driveshaft, resulting in a 1:1 speed ratio. This is a design change from the concept (Masters et al., 2022) which anticipated a gearbox and vertical shaft to a PTO on the barge deck. Placing the PTO underwater significantly reduces the cost and mechanical losses that would have been required for power transmission to the surface compared to the original geared option. The reduced rotation rates meant that the piston stroke and diameter were up-sized to a 440 mm stroke length and 6" diameter (7.8 l volume) so that turbine speed could still be controlled to optimum TSR by opening and closing the throttle valve.

The pump itself is primarily made up of a 6" thin-wall stainless steel manifold, four 4" PVC non return (ball check) valves and various threaded and flanged 4" pipe fittings as shown in Fig. 6. The manifold, pipe fittings and piston rod are supported by a rigid frame, allowing the entire pump to be transported as a unit. This was beneficial in transferring equipment between initial assembly and testing in the lab and the field. When deployed, the pump is aligned vertically and is fully submerged in the river. Consequently, the piston crank moving parts (i.e. crank rod and slide rails) use plain off-the-shelf bearings, and are lubricated by the river water.

2.3.5. Test platform

A 10×5 m barge was used as the test platform — the construction of the barge is discussed further below. At the rear of the barge was a pivoting and sliding arm with a load capacity in excess of 8 kN as shown in Fig. 7. The turbine was mounted on the bottom of the arm and was submerged at a hub depth of 3.5 m. The water pump PTO is attached the back of the arm as shown in Fig. 8. The crank and slider assembly is clearly visible in this Figure. Electrical equipment was housed inside a container cabin secured to the deck, and an electrical harness routed from the cabin down to the turbine driveshaft capsule via the submersible arm.

2.3.6. Safety shut-off brake

The primary turbine braking system is full closure of the throttle valve, creating enough hydraulic back pressure to stall the rotor. However, a shut-off brake was incorporated as a secondary means of preventing the turbine from rotating and also to act as a parking brake when the turbine was not being tested. The brake is operated from the top end of the arm and is accessible from the barge deck. The brake is triggered using a quick release shackle to activate a spring loaded lever which, in turn, pulls a brake cable and applies the brake clamps onto the driveshaft brake plate.

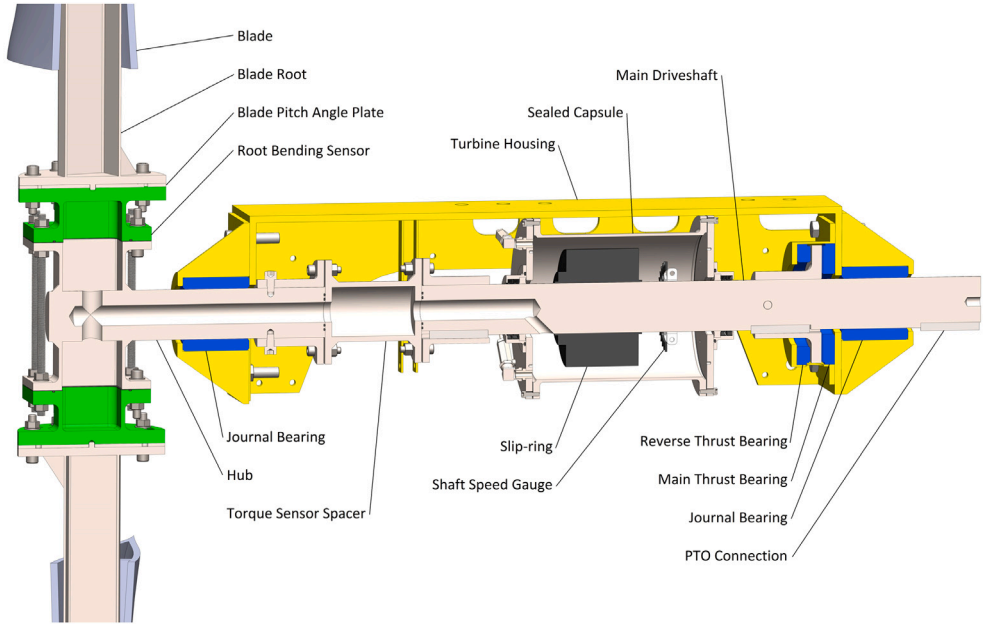

Fig. 4. RRES drivetrain section view.

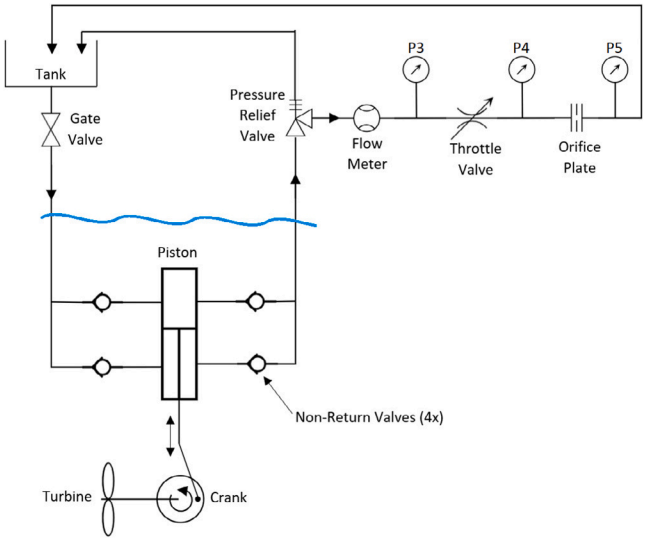

Fig. 5. RRES PTO Schematic. Additional pressure sensors P1, P2 were fitted across a non-return valve on the quarter scale laboratory rig.

Fig. 6. RRES PTO bench test in Swansea University. PTO system to the front of the bench, drive motor to far right, laboratory torque sensor inline but not visible behind crank attachment on right.

2.4. Instrumentation

Control and instrumentation of the RRES was provided using a range of off-the-shelf hardware, supplemented with custom software. The control system was designed to be usable for both laboratory and full scale testing, with only a few hardware adjustments and a software switch required to move between operating modes. The system was housed in a pair of IP67 rated industrial enclosures, with one dedicated to the motor drive required for laboratory testing and the other serving as the general control system.

The control software was based around the open source OpenPLC software project (Alves, 2023), running on a Raspberry Pi 3B+ single board computer. A second Raspberry Pi 3B+ was added for field trials in order to allow additional data input/output without risking the ability of the first unit to provide control functions. Several interface boards were used to provide sensor connections, including analog to digital converters (ADCs) to read voltage based signals, digital to analog converters (DAC) to provide variable voltage outputs and a number of digitally controlled relays — two of which provided control signals to the motor controller in the laboratory environment.

The full sensors list is described below, but included hydraulic pressures, drive shaft rotation, drive shaft torque, and (in the laboratory) recording of the motor drive parameters.

2.5. Moorings

The RRES used a 4-point mooring system; mooring lines were connected to each of the 4 corners of the barge to ensure the barge stayed aligned to the flow direction. Each of the 4 mooring lines was made up of a 1.5 tonne gravity anchor, a 25 m line of 2" chain and a 20 m riser rope. The moorings were configured as shown in Fig. 9, and more detail is available as part of the documents released with the platform and turbine design at Masters et al. (2023).

Fig. 7. Full scale turbine and pump assembled to test platform, side view.

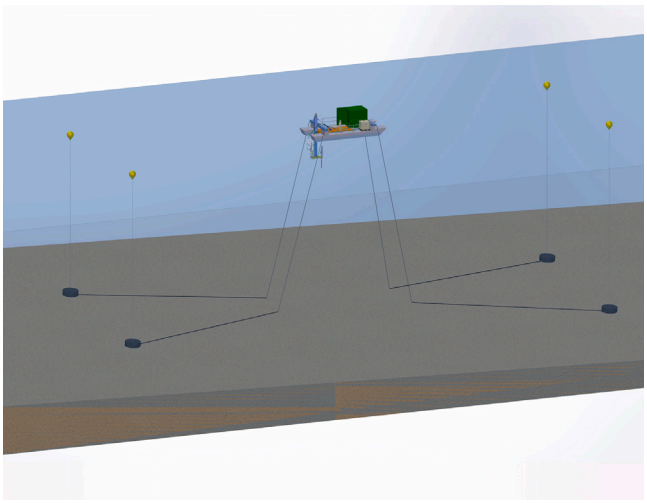

Fig. 9. RRES Mooring Configuration.

Fig. 8. Full scale turbine and pump assembled to test platform, rear view. Green control cabin to rear with the water storage IBC to the right of the cabin.

Fig. 10. Picture of the laboratory test rig.

A mooring design verification was performed by a third party company to ensure the proposed design was robust and appropriate for the predicted load cases on the barge and turbine. The moorings were laid during low tide slack water using a multicat vessel. For each of the four points, the gravity anchor was positioned on the seabed and then the 25 m chain laid down with marker buoys on the riser to allow the barge to be connected at a later date.

3. Laboratory preparatory experiments

3.1. Power take off

Similarly to the scaled test rig described in Evans et al. (2022), the full scale test rig was installed in the ESRI Coastal Lab at Swansea University. The full scale rig was designed to allow the PTO to be built *in situ* and transferred to site as a complete unit after disconnecting the crank and instrumentation connections. A photo of the bench test rig is shown in Fig. 10.

The lab mechanism uses a motor to provide input energy in a controllable manner, with an open loop hydraulic circuit drawing water from a barrel that can be replenished from the lab supply as required. An orifice plate is used near to the outlet of the hydraulic loop to simulate the pressure drop across a hydraulic generator.

Details of the required data measurements from various instruments are given in Table 3.

The test rig was tested across a range of motor input rotational speeds and torque to represent operational conditions, with some limitations due to the maximum power and current draw of the motor and motor driver. Each test lasted for 180 s, split into three stages. The first 30 s were used to ensure that the target motor rotational speed and pressure target were reached, and the period between 30 s and 60 s was used to allow the PTO to reach a steady operating state. The remaining two minutes were used to record data at 10 Hz frequency. Approximately 80 different speed and torque combinations were recorded.

Figs. 11 and 12 show 20 s time series of torque, pressure at P3, P4, and P5, pumped flow rate, and shaft rotation rate for two of the test cases. These test cases illustrate a low rotational rate and high rotation rate, both at high torque. Only 20 s of data is plotted for improved readability. The two test cases used both had the throttle valve at 20% open.

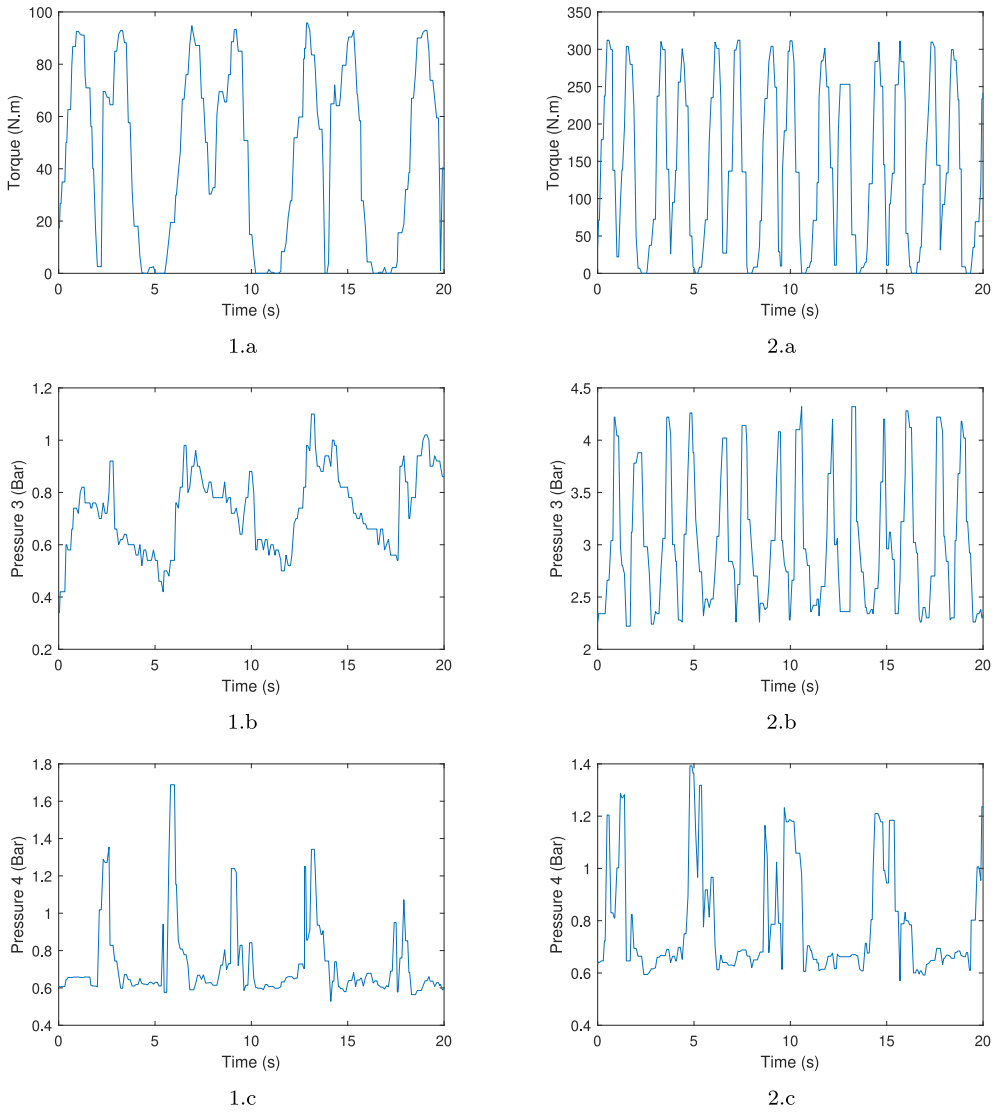

Fig. 11. 20 s time series plots (1) low and (2) high rotation rate, both at high torque with throttle valve at 20% open. Plots show (a) torque, (b) pressure at P3, and (c) pressure at P4.

Table 3
Detail of the sensors data measurement requirements for the full scale laboratory rig test program.

Instrument		Data measurement requirement
Name	No.	
Torque sensor	1	Torque and rotational speed of main shaft from motor
Flow rate sensor	2	Volumetric flow rate in piping system after the join of the outlet pipes
Throttle valve	3	Control and measure valve position
Pressure sensor P3	4.3	Pressure in piping system after the join of the outlet pipes and prior to throttling valve
Pressure sensor P4	4.4	Pressure downstream of throttling valve prior to restriction orifice
Pressure sensor P5	4.5	Pressure downstream of restriction orifice
Temperature probe	5	Temperature at inlet pipe

Fig. 13 shows plots of mean torque, rotational rate, flow rate, throttle valve position, and pressure measured at P3 (the sensor upstream of the throttle valve) with standard deviation error bands for all tests.

A contour plot showing torque against rotational rate and pressure at P3 is shown in Fig. 14. As expected, the torque is proportional to both the rotation rate and pressure upstream of the throttle. This pressure is increased by closing the throttling valve, narrowing the outlet pipe. If the rotational rate is kept constant and the pressure is increased, the torque also increases. Similarly, if pressure measured at P3 is kept constant and the rotational rate is increased, the torque also increases.

Similarly to Fig. 14, Fig. 15 considers the effects of throttle valve position on the same data and shows rotational rate and throttle valve position against torque. The plot is restricted to throttle valve positions <40%, as positions >40% made no noticeable difference to the recorded torque. It indicates that the system was not fully primed, i.e. full of water, and a significant proportion of the volumetric flow is air.

Power can be calculated at various locations on the laboratory test rig from measured data. The input power, P_{Input}, is calculated at the torque sensor using Eq. (1), where T is torque, and ω is rotational speed.

$$P_{\text{Input}} = T \times \omega \tag{1}$$

The power at location 3, P_3, can be calculated using Eq. (2), where p_3 is the pressure, and $\dot{v}$ is the volumetric flow rate.

$$P_3 = p_3 \times \dot{v} \tag{2}$$

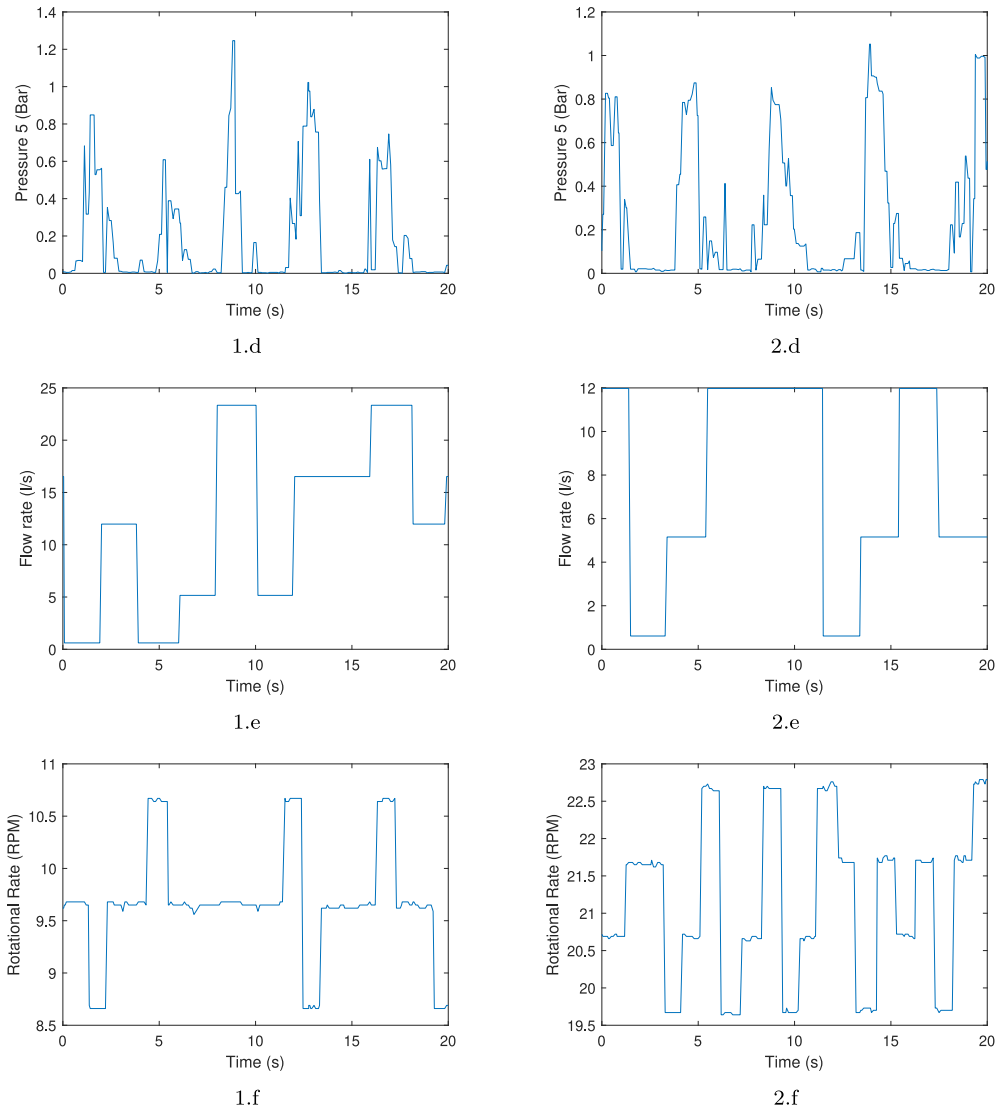

Fig. 12. Continued from Fig. 11 - 20 s time series plots for (1) low and (2) high rotation rate, both at high torque with throttle valve at 20% open showing (d) pressure at P5, (e) pump flow rate, and (f) rotation rate.

The efficiency of the PTO and pump can thus be calculated and is plotted in Fig. 16. The calculation of efficiency is only as accurate as the measured parameters. There is good confidence in the accuracy of the measured pressure at location 3 and torque, but not the flow rate. The spikes in efficiency are likely due to over-estimations of flow rate, exaggerated by large volume of air in the system.

The amount of air drawn through the system during lab tests was exacerbated by the water supply being located below the level of the pump. During field trials, the pump was located below the level of the reservoir during operation and the system could be primed by using a small external pump to fill the system. Based on the appearance of flow through the translucent pipework used, there was little air present in the outlet flow from the pump.

3.2. Blade root strain measurement

As described above, the blades were connected to the hub via machined blade root mounting adapters, which were designed to provide an internal dry space for instrumentation. Measuring forces acting on the blade using strain gauges has been successfully demonstrated on other occasions — with fibre optic based gauges as in Harrold and Ouro (2019), Lake et al. (2021), Marone et al. (2025) and with full-bridge gauges as in Allmark et al. (2020).

In this case the strain gauges were installed on the internal faces of each blade root mounting adapter in two half-bridge pairs — space constraints limited the ability to install a full bridge arrangement in this instance. The internal faces of the adapters are oriented such that one pair of strain gauges in each measures bending in the rotation direction (i.e. torque) and the other pair measures bending perpendicular to this and parallel to the driveshaft. No strain gauges were installed to measure blade twist. Each pair of strain gauges was connected to a combined amplifier and digital interface (Mantracourt DCell DLCSMOD) for connection to the control and logging system using RS-485. Each digital interface was configured with a unique ID, allowing the interfaces for each blade to share communication wiring.

Each blade root adapter was calibrated separately by bolting the base of the adapter to a bending rig previously used for blade testing and bolting a length of I-beam to the blade mounting face. A load was applied to the beam using a hydraulic ram, connected via steel rope and a pulley with a calibrated load cell at the connection point. The load cell output was measured using a digital multimeter, and the output of the strain gauges being calibrated was read from the digital interface.

A load was applied to the beam in increments from zero until the target pressure was indicated on the hydraulic ram, with a pause after each load application to allow the multimeter readout to settle.

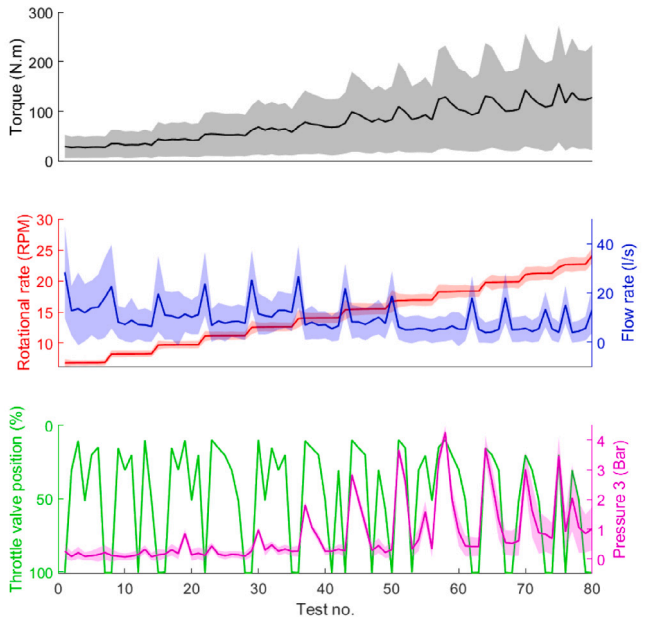

Fig. 13. Plots of mean torque, rotational rate, flow rate, throttle valve position, and pressure at P3 with standard deviation error bands for all tests.

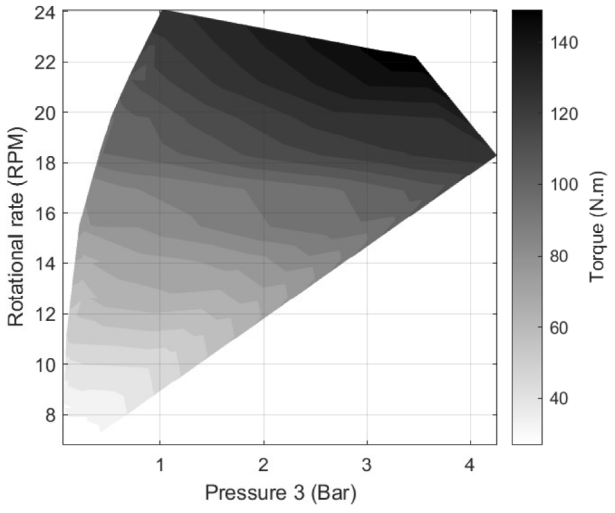

Fig. 14. Contour plot of rotational rate and pressure at P3 against torque.

After the target was reached and values recorded, the pressure in the hydraulic ram was released and an additional set of values recorded. This process was repeated at least once more before rotating the blade root mounting adapter. The full procedure was carried out in three orientations — the original mounting position (taken as 0°), when rotated by 90° and by 180° (clockwise when viewed from the blade mounting face in both instances). Due to time constraints, the logical fourth position of 270° clockwise from the start point was omitted after initial inspection of the recorded data.

A least squares fit between the measured strain gauge outputs and the applied load provided coefficients for conversion from strain gauge output to an equivalent load.

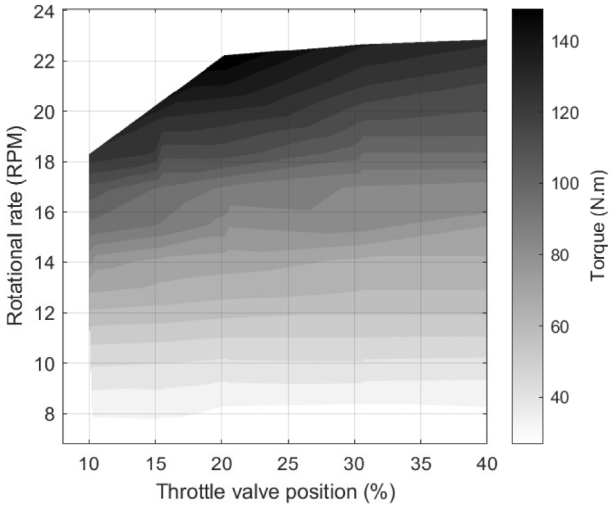

Fig. 15. Contour plot of rotational rate and throttle valve position against torque.

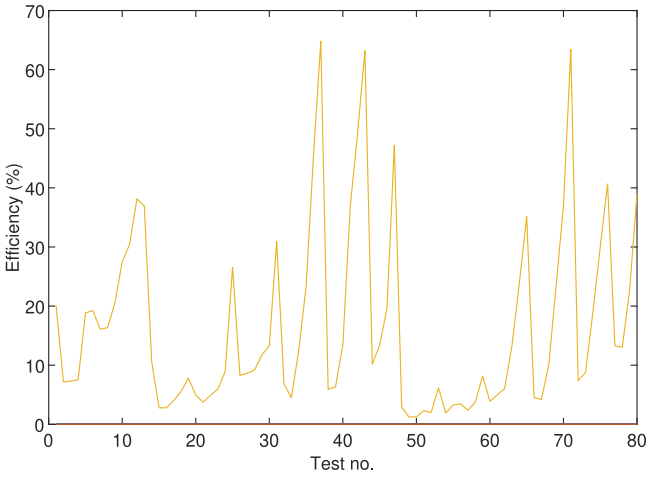

Fig. 16. Plot of the PTO and pump assembly efficiency.

4. Field experimental method

The test programme was conducted across three separate campaigns, where the purpose of each campaign was to trial various aspects of the system.

1. Completed barge, installed on the moorings with a smaller 1 m diameter turbine rotor. The aim of this test was to verify the barge system, troubleshoot the control and data electronics and gain some learning into the marine operations. It was conducted in February 2023.
2. A short term tow test, with the full scale rotor and PTO, to validate the system. The tow trial was carried out in May 2023, with the full scale RRES towed behind a workboat on the estuary. For this trial deployment an increase of 10 degrees to the pitch angle was used to ensure the turbine would overcome the inertia in the PTO system during start-up. This was successful and a zero degree angle used during subsequent tests.
3. A longer term moored test, to gather the full system performance data. This was carried out in January and February 2024.

Operational planning required significant consultation with the site operator, vessel contractors and the harbourmaster. Risk Assessment

and Method Statements (RAMS) were formulated prior to the anchored deployment and the tow trial deployment. The RAMS covered all aspects of the operations, including; RRES assembly, mooring installation, RRES mobilisation, operating and testing the RRES, demobilisation and decommissioning.

The test platform was constructed from two 10×1.5 m pontoons, which are 2 m apart and rigidly connected by two heavy duty steel beams (one front and one rear). A 6800 l float is fixed between the pontoons for additional buoyancy and to form a larger deck area. The turbine arm is assembled at the rear end of the barge as shown in Fig. 7, a hydraulic ram allowed the arm to pivot on the rear steel beam, and a steel cable manual winch (Tirfor) was used to slide the arm up and down through a boom. The test platform was assembled and turbine, PTO and electrical equipment fitted and commissioned at Rudders Boatyard, approximately 2 km from the test site. Site services including the slipway and pontoon were used by the project. Boatyard staff supported the build through use of telehandler for lifting, launching of support vessels and interaction with the marine contractors.

5. Results

The turbine instrumentation consisted of the flow meter and pressure sensors used in the lab tests, with the addition of the blade root strain gauges, a hall effect encoder and toothed wheel for measuring shaft speed and a Nortek Vector ADV to provide an upstream flow speed measurement in realtime. The ADV was located on the starboard side of the barge and positioned so that readings were parallel with the rotor level with the minimum blade tip depth. The data was recorded independently at 16 Hz, with a subset of this data recorded live by the control system. The flow speed was presented to operators for information as both the instantaneous value and as rolling 10 and 2 min averages, alongside calculated tip speed ratios for each average. In response to this data, operators manually selected various throttle valve positions to create varying pressure loading on the system. The control system did not contain any programmed responses to the ADV data, although that could be implemented in future. Additional temperature, humidity, and pressure measurements from inside the shaft mounted electronics enclosure were recorded to provide a measure of warning in the event of water ingress into the enclosure.

As well as the operational sensors, four bottom mounted acoustic doppler current profilers (ADCPs) were deployed on January 16th, with a fifth downward facing unit installed on the platform and enabled on January 25th. These were all synchronised to UTC prior to deployment, but operated independently throughout the test. The ADCPs were configured to record at 4 Hz for 20 min every half hour, with the exception of ADCP 4 which was positioned on the north/channel side of the mooring and configured for 2 Hz recording of both current and wave data. All ADCPs were configured to use a 0.5 m bin height, and one pair of units had the recording times offset by ten minutes to provide around the clock coverage.

The final part of the monitoring setup for this deployment included a pair of Garmin eTrex 10 GPS recorders, which were located on the forward starboard corner of the shipping container and in a corresponding position on the rear steel beam to provide position data and an alternative measure of the platform's orientation during the test — the ADV and platform mounted ADCP both already containing on board magnetometers.

The use of surface mounted ADV, and surface and bed mounted ADCPs allows for further comparison between these device types with regards to their use on floating tidal platforms, building on previous comparisons reported in Frost et al. (2022). This is planned as future work by the authors.

5.1. Data availability

The moored test of the full scale system took place between January 25th and February 5th 2024, the results of which are presented here. After commissioning the turbine and constraints due to weather, seven working days were available for data collection, with operations limited to daylight hours and further constrained operations to ebb tides only by the mooring arrangement and fixed rotor and blade orientation. These days are listed in Table 4, along with a summary of the days activity. As stated in the table, a bearing failed on the crank mechanism linking the driveshaft to the pump piston slider. Replacement of this part could not be made in time for an turbine operation on January 30th.

On all other operational days, after startup the turbine was allowed to run under varying throttle conditions until flow speed was insufficient to keep the turbine rotating.

Operational data was recorded whenever the control system was powered, which includes all times where the turbine was operating as well as some idle/non-operating time before and after operations. The positions recorded on the GPS units were intended to give continuous coverage but were limited by poor battery life, with gaps over periods where the platform was uncrewed and batteries could not be replaced. At least one GPS unit was recording during all times that the turbine was operating.

The ADCP records are continuous between deployment and recovery, with the platform mounted ADCP recording between 15:10 on January 25th and 15:40 on February 5th and the seabed mounted instruments all recording between 16:20 on January 16th and 08:50 on February 14th.

Some sensors failed on deployment, with subsequent limitations on data availability. Specifically:

- Pressure sensors
- Shaft speed sensor
- Pump output flow rate

After seeing no realistic signals recorded from the pressure sensors, two of the three sensors were replaced with spares on February 1st, recording pressures before and after the throttle valve. Unfortunately no further spares were available, meaning that pressure after the orifice plate was not recorded.

The failure of the shaft speed sensor was identified at the start of data collection, and is believed to be due to movement of the sensor relative to the toothed wheel. As an initial mitigation, the shaft speed was recorded manually based on observation of the pump action. Post-processing data to apply a peak counting algorithm over 2 min chunks of data yielded values matching these manual measurements, and has been used to derive RPM data for analysis. The same process was adapted and applied to a two minute rolling sample of data to allow for a live readout during the deployment.

5.2. Operational data

Turbine operating data has been processed following the methods outlined in IEC technical standard 62600-200 (IEC, 2013), using both two minute and ten minute averages and 0.10 ms^{-1} velocity bins. For brevity, bins will be labelled using the midpoint value — i.e. the velocity bin covering average flow speeds equal to or greater than 0.50 ms^{-1} but less than 0.60 ms^{-1} will be referenced as the 0.55 ms^{-1} bin.

The distribution of these bins against the mean flow speed measured by the ADV is shown in Fig. 17, split between times where the turbine was operating (orange) and times where the system was monitoring but the turbine was not operating (blue). As seen in the figure, the turbine operated in the highest observed flow speed bin (1.15 ms^{-1}) down to 0.6 ms^{-1} when averaged over ten minutes or 0.55 ms^{-1} when averaged over two minutes.

Table 4
Available operational (ops) days and summary of activity.

Date	Reference	Summary
26/01/2024	Ops Day 1	Run until rotor stalled at low flow speed
29/01/2024	Ops Day 2	Run until mechanical failure of crank mechanism
30/01/2024	–	No operations – repairs made.
31/01/2024	Ops Day 3	Return to operations. Run until stall.
01/02/2024	Ops Day 4	Run until stall
02/02/2024	Ops Day 5	Run until stall
05/02/2024	Ops Day 6	No running – neap tide with peak flow below cut-in speed

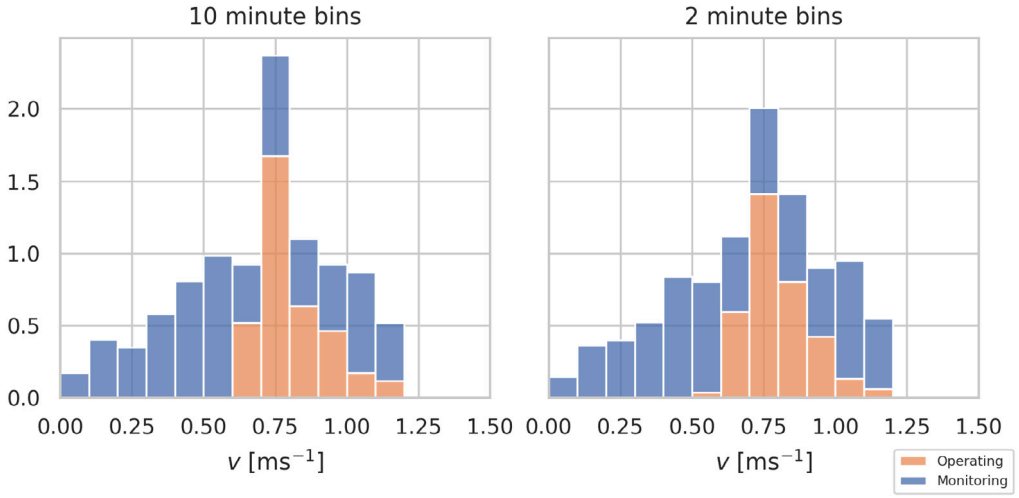

Fig. 17. Histogram of recorded mean flow speeds for 10 min and 2 min bins, coloured by operating state. The data is normalised such that the total area equals one.

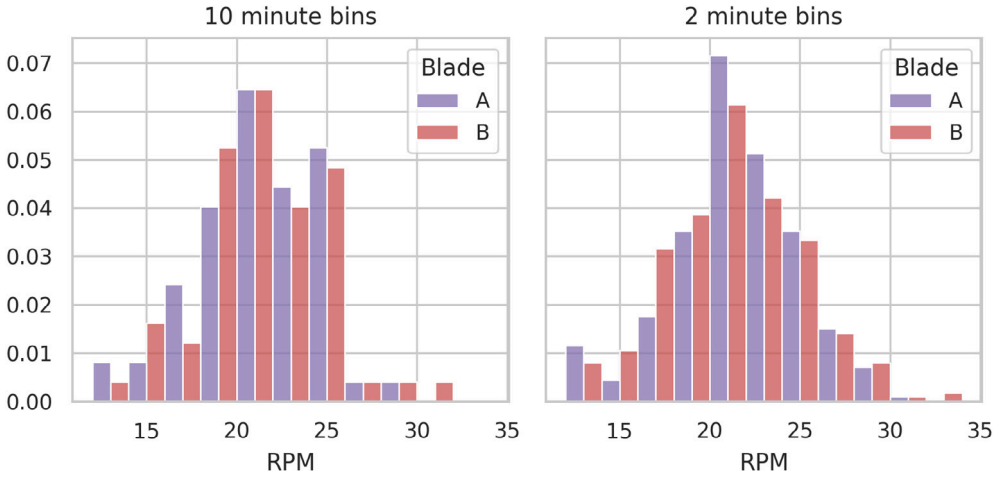

Fig. 18. Histogram of turbine RPM derived from strain gauge data, coloured by blade used to derive speed. The data is normalised such that the total area of each colour equals one.

As described above, the original RPM measurement sensor provided no data during the deployment but RPM could be derived from the strain gauge data on each blade. These derived values are shown in the histogram in Fig. 18, with the bars coloured based on which blade's strain data was used to calculate RPM. The distributions are very similar, but with the blade A data showing very slightly slower speeds — this is more obvious in the plot of two minute averaged data, but still represents a small number of bins. All other quantities calculated based on RPM are labelled or coloured in the same manner unless stated otherwise.

The tip speed ratio (TSR) of a turbine is often used to illustrate operation and a histogram of tip speed ratios achieved for this test is shown in Fig. 19, showing ten minute average bins from 2.75 to 4.75 (and a single outlying bin at 6.25) and two minute average bins between 2.25 and 4.75. This range covers the design optimal value (4.5) and most of the test scenario TSRs listed in Table 1, and would be consistent with the turbine operating at its optimal TSR for most of the operating time.

Moving from overall distributions of data to timeseries, Fig. 20 shows the two minute (dotted) and ten minute (solid) averages of recorded flow speed alongside RPM and TSR calculated from the blade B strain data. Each operational day is plotted as against time from predicted high water, to allow comparison between days. Data recorded on January 29th is not shown, as insufficient data was available due to mechanical failure. As shown in the figure, the flow speed decreases each day as the ebb tide progresses towards low water but the rate of this change is small — giving consistent conditions for testing. The RPM (and therefore TSR) values are affected by control settings as well

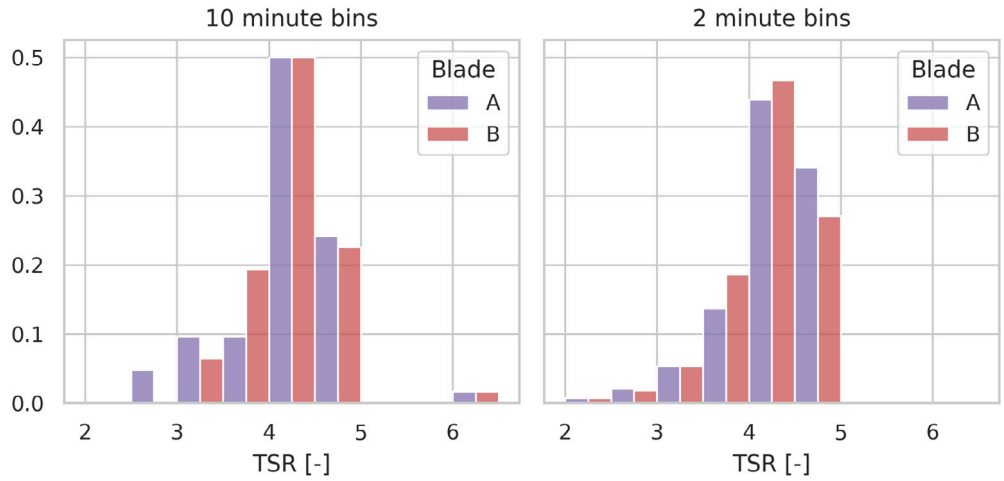

Fig. 19. Histogram of turbine tip speed ratio (TSR), coloured by blade used to derive RPM. The data is normalised such that the total area of each colour equals one.

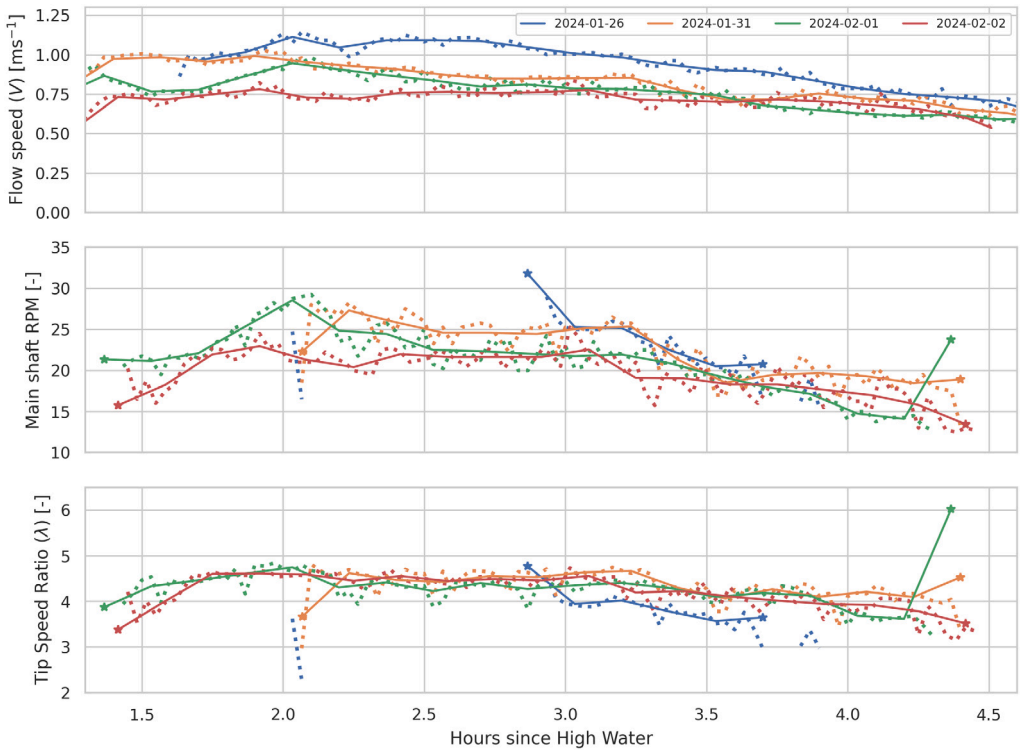

Fig. 20. Recorded flow speed, RPM, and TSR (both from blade B strain data) plotted against hours from that day's predicted high water time. Dotted lines show two minute averages, solid lines represent ten minute averaged data.

as variation in flow speed, but it can be seen that the general trend is for the RPM to decrease during each tide as the flow speeds drop. The increased RPM shown as the final ten minute average on February 1st is inconsistent with the two minute data and is likely to be a spurious value — with the turbine stopped there is no periodic signal present in the strain data, and the calculated RPM is likely influenced by noise in the sensor recording. It can be seen that this single point also results in the single bin of data at TSR = 6 noted in Fig. 19.

Continuing with the time series data, Fig. 21 shows two minutes of data recorded between 12:59 and 13:01 on February 1st 2024. The throttle control was held at a constant value of 50% throughout this period. This figure shows the recorded flow data from the ADV, the calculated RPM values, pressure data before (3) and after (4) the throttle valve, and the torque and thrust direction bending moment calculated from the strain gauges. The figure illustrates the rapid fluctuations in flow speed and the turbine response to these fluctuations, with the most obvious feature being the acceleration in flow speed at 12:59:45, followed by an increase in torque and measured pressures in the pump outlet line. The two minute averages also show the decrease in shaft RPM corresponding to a reduction in the two minute average flow speed, as would be expected in the absence of throttle valve changes.

The thrust and torque data shown in Fig. 21 also illustrates a problem in the recorded data that was only noted post-deployment — the scaling of recorded strain data into the required torque and thrust values is not correct and leads to physically implausible values. This will be discussed further below, but can be seen here in the diverging behaviour of the blade data in the thrust plot — even if the individual values differ, the trend observed in both blades should be in the same direction.

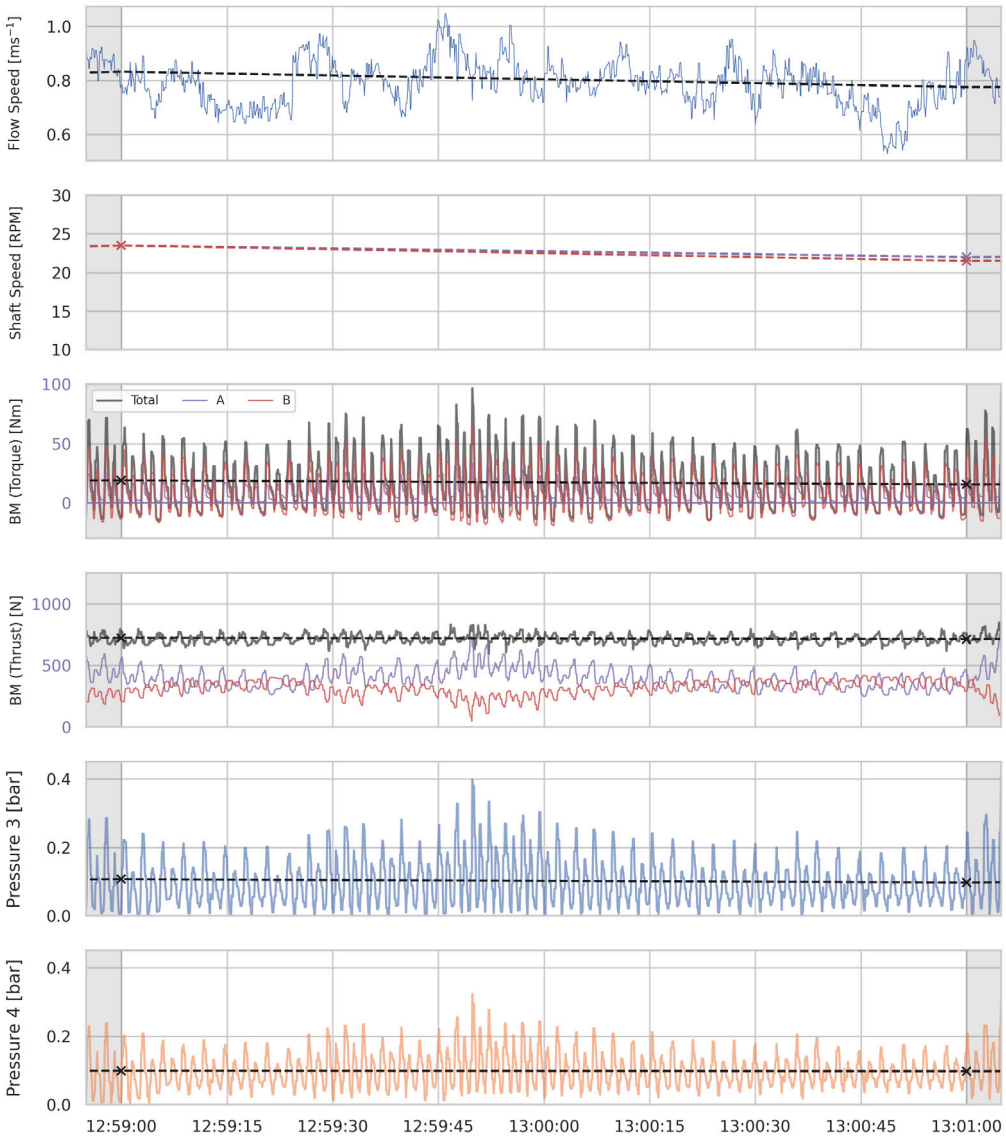

Fig. 21. Turbine operational data recorded between 12:59 and 13:01 on February 1st 2024. Dashed lines join two minute average values centred on corresponding X marks.

The plot in Fig. 22 shows the power calculated from the torque and RPM derived from each blade's strain data for each velocity bin, with data presented for both the ten minute averaged and two minute averaged bins. These values fall significantly below the expected values — the expected mechanical power was expected to be 740 W for an inflow of 0.8 ms^{-1}.

This discrepancy is further illustrated when looking at the non-dimensional coefficients of power, shown in Fig. 23. The plots of power coefficient in Fig. 23 do not show a clear peak, which is consistent with the histogram shown in Fig. 19 — the relatively low flow speeds seen during the test limited the ability to test the turbine at higher TSR values. The highest complete TSR bins (4.25 and 4.75) cover the design optimal TSR and may capture the peak C_P value, but further tests would be required to be confident in this.

6. Discussion

6.1. Project cost summary

One aspect of prototype development that is often neglected is the actual costs of undertaking a project. The input of the project staff is the most important part of any project and we estimate that around 3–4 person years of effort were expended to deliver the unit and the test programme. Excluding salaries, the total project cost was £155,000 (excluding VAT). This covers all purchases and services that were required for the design, build and testing of the RRES. Some technical services provided by Swansea University were not included in this estimate, which included workshop time for part adjustments and alterations, 3D printing facilities and in-house marine survey expertise. Support teams involved were project administrative staff, the procurement department, and legal services for review of the test site agreements and insurance cover.

The build was conducted just after the COVID-19 pandemic and supply chains were still constrained for some items, in particular shortages and delays were a factor for electronic components. Efforts were also made to encourage the local supply chain to bid for any work tendered. This was partly due to the regional nature of the project funding and partly to improve the quality of the subcontract parts delivered. The largest costs were prototype parts, barge modifications and hire, and marine operations. A significant proportion of the cost was due to sensors and electrical parts required to instrument the device for research purposes. These may not be necessary for a production turbine. Some standard oceanography sensors have been used (ADVs in particular) and the cost of these units is not included. Fig. 24 shows a breakdown of the project costs into various categories.

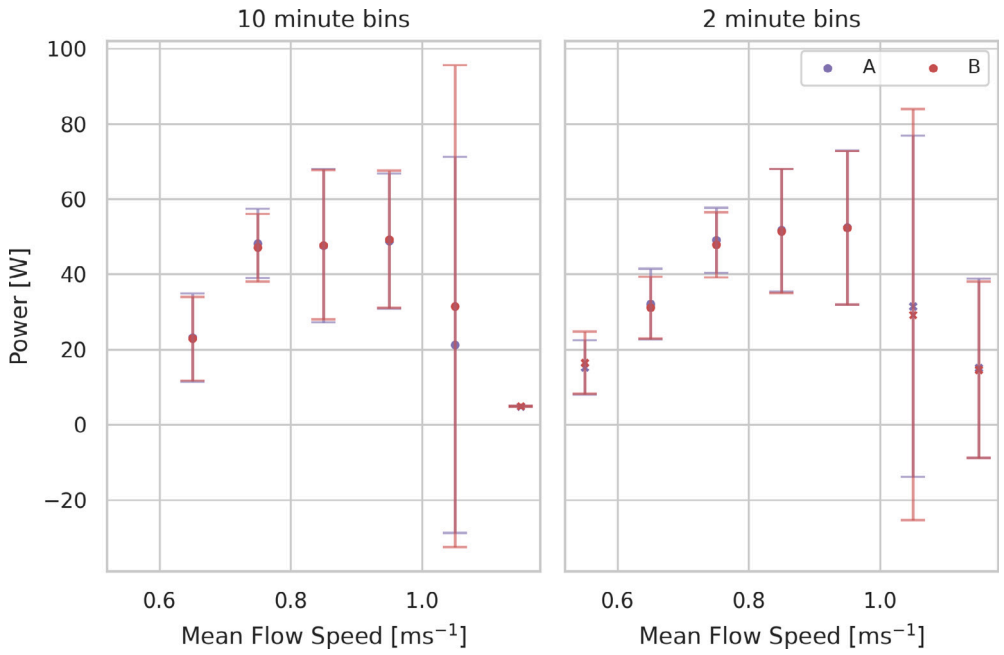

Fig. 22. Calculated mean rotor power plotted against flow speed for ten minute and two minute averaged data. Points plotted X contain less than 30 min of data, error bars represent one standard deviation.

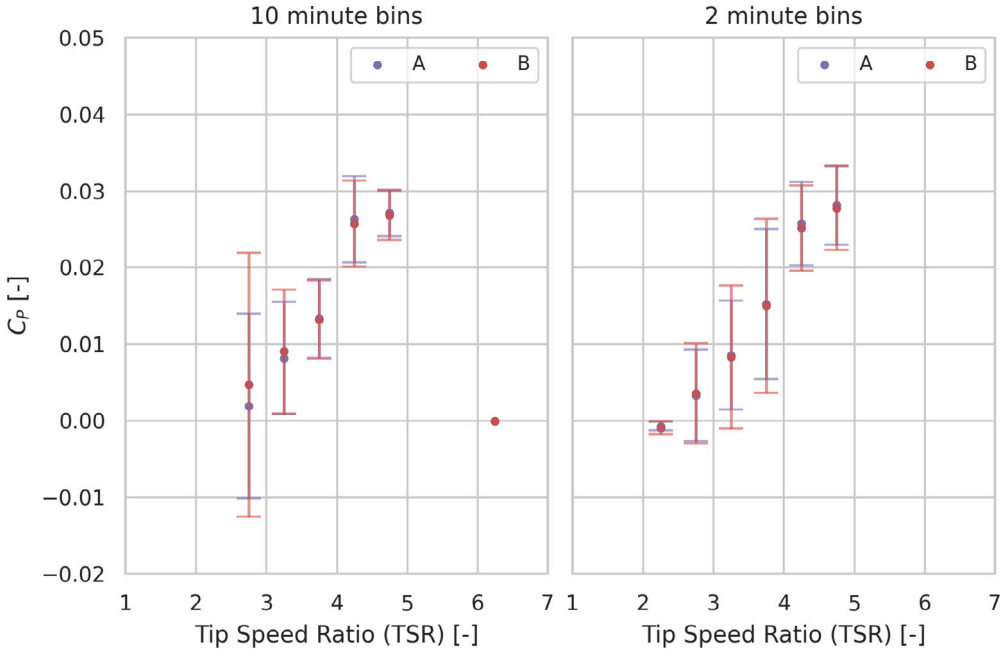

Fig. 23. Coefficient of power (C_P) plotted against tip speed ratio (TSR).

6.2. Operational performance

The available data from this deployment suffers from a number of limitations, most of which were identified and remediated (where possible) during the deployment. The available data provides information about the inlet flow during operation, and shows that the turbine was able to operate in flow speeds with a ten minute average above 0.65 ms^{-1} (or a two minute average above 0.55 ms^{-1}). Operation was also demonstrated over a wide range of rotation speeds, as illustrated in Fig. 18. The trial period coincided with a period of neap tides, and lower flow speeds were encountered during the available operating period, meaning that the rated design speed of 38 RPM was not reached, although the ability of the device to function in low flows was successfully demonstrated.

The mechanical water pump operated successfully, with estimated flows up to 140 l min^{-1}, although further characterisation is difficult without more consistent flow and pressure data being available. The pump was noted to be noisy during operation, even after repairs made to the crank mechanism. This noise likely indicates excess friction due to misalignment in the mechanism, possibly due to the length of unsupported shaft within the piston at the top dead centre position (when the crank connection is closest to the cylinder end seal — these being the only two points that the piston shaft is supported). The fluctuations visible in the pressure sensors could be mitigated by a hydraulic accumulator or other pressure regulator as used in other

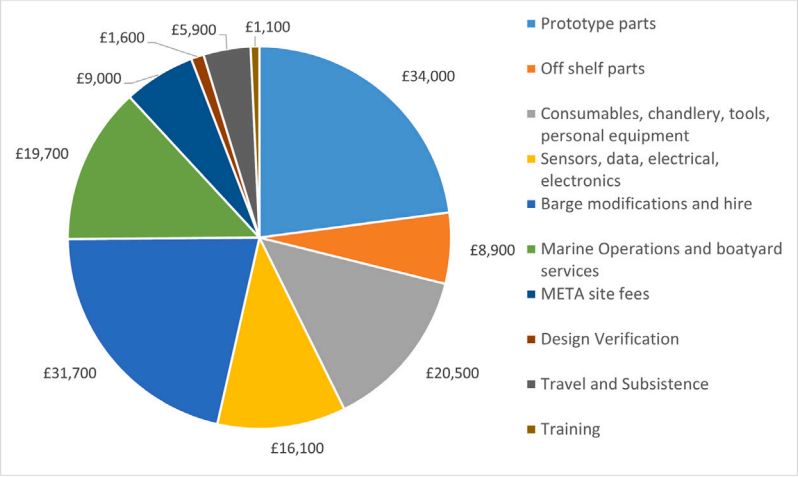

Fig. 24. Actual costs of trial, GBP ex-VAT as valued in 2022. Does not include staff time, procurement, legal advice and insurance.

low cost water pumping applications (Fraenkel and Thake, 2006). This element of the mechanism will be considered for redesign in future work.

In Fig. 21, a high-low pattern can be seen in both the strain gauge and pressure data. This is thought to be due to the friction in the crank mechanism described above, with the high-low pattern corresponding to the push and pull strokes of the piston. Trapped air within the pump cylinder has also been suggested as a possible cause for this pattern, which cannot be excluded without additional data. During field testing the outlet flow appeared consistent with few bubbles and no large volumes of air after initial startup — this was not the case during lab testing, as described above.

The overall operational data is limited to 9 h and 14 min of run time, principally acquired over ops days 3, 4, and 5. Although ops day 1 was run until the turbine stalled (including a brief additional period where it restarted before stalling again), the ten minute averaged flow speed at stall was 0.819 ms^{-1} (0.894 ms^{-1} over a two minute average). After repair of the crank mechanism following its failure on day 2, the turbine then ran until stall on the remaining three days, with an flow speed at stall between 0.681 ms^{-1} and 0.597 ms^{-1} based on ten minute averages (0.656 ms^{-1} - 0.601 ms^{-1} based on two minute averages). This may suggest that the higher stall speed was a result of the impending failure, although as this occurred on day 1 of the test it could not have been used as a warning at the time.

6.3. Strain measurement

The most significant issue with the data gathered is to be found in the strain gauges fitted to the blade root mounting adapters. While these strain gauges had been tested and calibrated in the lab, the data returned showed plausible trends but did not scale to expected values when the lab calibration coefficients were applied. Post-deployment, the turbine was returned to the lab and attempts were made to recalibrate the strain gauges by applying measured loads to each mounting adapter (the blades were removed on site and were not included as part of this process) with the power take off crank used to secure the main shaft and prevent rotation of the assembly. Note that while this limited the number of directions that could feasibly be loaded compared to the single unit tests, it allowed measurement of the strain gauge responses from both blade root mounting adapters simultaneously and with all components connected in their as-deployed state.

During this process, two key findings were made:

1. A filtering algorithm was enabled on the strain gauge amps that was not accounted for; this will have smoothed smaller variations in strain, but should not have obscured larger variations.
2. The four sets of strain gauges were not as independent as they should have been.

While in theory the two sets of gauges on each adapter were orthogonal to each other and aligned with the expected torque and thrust loads independently, a certain amount of coupling between them was expected and accounted for by calibrating each adapter as a unit rather than each pair of gauges in isolation. The unaccounted for issue lay in mechanical coupling of loads from one side of the hub to the other, such that a load applied in torque or thrust on one adapter would result in a smaller but still measurable load on the gauges in the other. Repeated lab tests were carried out including applying loads to each adapter in the torque and thrust directions, applying a load to both adapters simultaneously, and combined static loading of one blade while applying a variable (but measured) load to the other. The conclusion of these tests was that the resulting coupling was non-linear and while the signals from each gauge could be linearly scaled to the known loads applied, no numerical solution was found to correctly resolve the recorded signals to the correct loads for all scenarios tested. The data presented in this paper uses the original lab calibration values — while these yield incorrect results, they reflect the values during the deployment before the limitations became clear.

In order to minimise the impact of this problem for future deployments, it is intended to redeploy the turbine with a torque sensor fitted to the main drive shaft as per the original design intent. The hub will be reinforced and the strain gauges recalibrated after assembly. The undesired filtering process applied by the strain gauge amplifier/digitiser modules has been deactivated, which should allow smaller scale variations in strain to be more accurately recorded, allowing trends and correlations with other signals to be examined even if scaling factors are not correct.

The consequence of this issue means that the bending moments, and overall torque and thrust values from this deployment cannot be considered reliable, and as a consequence neither can derived quantities of power (and consequently C_P). The trends in averaged values and values derived from them is expected to reflect the correct overall trend, but this cannot be guaranteed.

7. Conclusions

Results presented here are a contribution to the science of small axial flow turbines on a number of levels. These will be considered in turn below.

This test programme has provided important information related to the development of a tidal/river turbine prototype and has significantly advanced the technology through to Technology Readiness Level (TRL)

5 on the EU Horizon scale. This is "technology validated in a relevant environment"; however, we believe the number of operational hours are not sufficient to claim TRL6 "technology demonstrated". In line with the methods of the original design concept in Masters et al. (2022), the design drawings for the unit tested here are published open source at https://zenodo.org/doi/10.5281/zenodo.8082024 and it is the authors wish that others will take on the design and progress it further in the future.

A reciprocating pump design has been tested and shown to be a potential power take off for river turbine technology. The fully mechanical system has shown to operate successfully in flows lower than those typically targeted by electricity generating tidal stream turbines. However, there are limitations related to the surface finish of the pump internal diameter, so that pumping efficiency is lower than expected.

Due to the layout of the strain gauge sensor systems, the four sets of gauges interact mechanically and it is not possible to obtain reliable measurements from the recorded data. The overall trends of power and torque coefficient are as expected and therefore there is some evidence of the system concept, but the available data is not sufficient to confirm the energy extracted during the tests.

The use of local supply chains has been successful, and a number of companies are now more familiar with offshore renewable energy technology. More specifically and related to the META site, there is now a proven methodology for operation of a tidal turbine on the site. The availability of a floating platform with a hydraulically operated arm will now facilitate further test programmes on the site. The combination of moderate flows, shelter from the worst wind and wave conditions and the very short distances to several boatyards means this is a very attractive site for early stage at sea testing.

7.1. Future work

There are clearly additional improvements that could be made to the pump layout and this will provide several research and development directions in future. The single cylinder and crank has an inherent issue that twice per revolution, the applied torque is perpendicular to the pump load direction and hence is effectively zero. A multiple cylinder system would smooth this pulse but require additional cylinders and valves. There is also the possibility of the use of a more conventional electrical machine as an alternative.

Another future stage of work would be to develop a production version of the design. The unit as it stands is a combination of an instrumented experiment and a proof of concept. The next step would be to remove the instrumentation, simplify the design and conduct a new trial with an aim of TRL 6 or 7.

Data collected by the co-located ADV and set of ADCP sensors will be analysed to give a very high resolution description of the flow around the barge.

Finally, the project team look forward to using the capability of the platform to support other projects and technologies.

CRediT authorship contribution statement

Ian Masters: Writing – review & editing, Supervision, Methodology, Funding acquisition, Conceptualization. **Ali Esmaeili:** Investigation. **Iestyn Evans:** Writing – original draft, Visualization, Investigation. **Deepak George:** Writing – original draft, Investigation. **David Glasby:** Writing – original draft, Project administration, Methodology, Investigation. **Jose Horrillo-Caraballo:** Investigation. **Thomas Lake:** Writing – review & editing, Visualization, Software, Investigation, Formal analysis, Data curation. **Dawn Morgan:** Investigation. **Michael Togneri:** Supervision, Software, Methodology, Funding acquisition. **Alison J. Williams:** Supervision, Methodology, Funding acquisition.

Declaration of competing interest

The authors declare the following financial interests/personal relationships which may be considered as potential competing interests: Ian Masters reports financial support was provided by MEECE project funded by the European Regional Development Fund. Ian Masters reports financial support was provided by UK Welsh governments through the Swansea Bay City Deal. If there are other authors, they declare that they have no known competing financial interests or personal relationships that could have appeared to influence the work reported in this paper.

Acknowledgements

This work was supported by the MEECE project funded by the European Regional Development Fund and the UK & Welsh governments through the Swansea Bay City Deal.

Data availability

Remote River Energy System (RRES) Field Trial - Full Scale device at Warrior Way, Marine Energy Test Area (META) - 01/2024 to 02/2024 (Original data) (zenodo)

References

Allmark, M., Ellis, R., Lloyd, C., Ordonez-Sanchez, S., Johannesen, K., Byrne, C., Johnstone, C., O'Doherty, T., Mason-Jones, A., 2020. The development, design and characterisation of a scale model Horizontal Axis Tidal Turbine for dynamic load quantification. Renew. Energy 156, 913–930. http://dx.doi.org/10.1016/j.renene.2020.04.060.

Alves, T., 2023. OpenPLC Runtime version 3. URL: https://github.com/thiagoralves/OpenPLC_v3.

Bhui, K., Hazra, S., Bhadra, T., 2025. Assessment of tidal energy potential from low-velocity tidal flows in the Indian sundarbans utilizing validated hydrodynamic model and tidal turbine technology. Renew. Energy 242, 122410. http://dx.doi.org/10.1016/j.renene.2025.122410, URL: https://www.sciencedirect.com/science/article/pii/S0960148125000722.

Coles, D., Angeloudis, A., Greaves, D., Hastie, G., Lewis, M., Mackie, L., McNaughton, J., Miles, J., Neill, S., Piggott, M., Risch, D., Scott, B., Sparling, C., Stallard, T., Thies, P., Walker, S., White, D., Willden, R., Williamson, B., 2021. A review of the UK and British channel Islands practical tidal stream energy resource. Proc. R. Soc. A Math. Phys. Eng. Sci. 477 (2255), http://dx.doi.org/10.1098/rspa.2021.0469.

Evans, I., Glasby, D., Lake, T., Togneri, M., Masters, I., 2022. Experiments in the ocean: Development of a small-scale sea trial tidal turbine test rig. In: Trends in Renewable Energies Offshore. CRC Press, pp. 133–142.

Fraenkel, P., Thake, J., 2006. Water Lifting Devices: a Handbook for Users and Choosers, third Ed.

Frost, C., Togneri, M., Jeffcoate, P., Lake, T., Boake, C., Starzmann, R., Williams, A., 2022. A comparison of platform and sea-bed mounted flow measurement instrumentation for SME PLAT-I. Int. Mar. Energy J. 5 (2), 195–200. http://dx.doi.org/10.36688/imej.5.195-200.

Grattan, K., Noble, D.R., Jeffrey, H., 2024. UK Ocean Energy Review 2024. Technical Report, Policy and Innovation Group, The University of Edinburgh.

Harrold, M., Ouro, P., 2019. Rotor Loading Characteristics of a Full-Scale Tidal Turbine. Energies 12 (6), 1035. http://dx.doi.org/10.3390/en12061035.

IEC, 2013. Electricity Producing Tidal Energy Converters - Power Performance Assessment. Standard IEC TS 62600-200, International Electrotechnical Commission.

Kirke, B., 2019. Hydrokinetic and ultra-low head turbines in rivers: A reality check. Energy Sustain. Dev. 52, 1–10. http://dx.doi.org/10.1016/j.esd.2019.06.002.

Lake, T., Glasby, D., Horrillo-Caraballo, J., Togneri, M., Masters, I., Austin, M., Lincoln, B., 2024. A low-cost, high-fidelity converging-beam Doppler instrument for measuring velocity and turbulence at tidal energy sites. Int. Mar. Energy J. 7 (1), 11–24. http://dx.doi.org/10.36688/imej.7.11-24.

Lake, T., Hughes, J., Togneri, M., Williams, A.J., Jeffcoate, P., Starzmann, R., Kaufmann, N., Masters, I., 2021. Strain gauge measurements on a full scale tidal turbine blade. Renew. Energy 170, 985–996. http://dx.doi.org/10.1016/j.renene.2021.01.137.

Lewis, M., O'Hara Murray, R., Fredriksson, S., Maskell, J., de Fockert, A., Neill, S.P., Robins, P.E., 2021. A standardised tidal-stream power curve, optimised for the global resource. Renew. Energy 170, 1308–1323. http://dx.doi.org/10.1016/j.renene.2021.02.032, URL: https://www.sciencedirect.com/science/article/pii/S0960148121001993.

Marone, N., Barrington, M., Gunawan, B., McEntee, J., Wosnik, M., 2025. Performance of cross-flow turbines with varying blade materials and unsupported blade span. Renew. Energy 238, 121925. http://dx.doi.org/10.1016/j.renene.2024.121925.

Masters, I., Bird, J., Birch, B., Reader, M., Turner, W., Holland, T., Lake, T., Williams, A.J., 2022. Remote river energy system: An open source low maintenance turbine design for remote areas. Proc. Inst. Civ. Eng. Energy 175, 64–80.

Masters, I., Evans, I., George, D., Glasby, D., Horillo-Caraballo, J.M., Lake, T., Togneri, M., Williams, A.J., 2023. RRES: A Remote River Energy System. CAD Model and Design Information. Zenodo, http://dx.doi.org/10.5281/zenodo.8082025.

Mycek, P., Gaurier, B., Germain, G., Pinon, G., Rivoalen, E., 2014. Experimental study of the turbulence intensity effects on marine current turbines behaviour. Part I: One single turbine. Renew. Energy 66, 729–746.

Neill, S.P., Fairley, I.A., Rowlands, S., Young, S., Hill, T., Unsworth, C.A., King, N., Roberts, M.J., Austin, M.J., Hughes, P., et al., 2023. Characterizing the Marine Energy Test Area (META) in Wales, UK. Renew. Energy 205, 447–460.

Togneri, M., Pinon, G., Carlier, C., Bex, C.C., Masters, I., 2020. Comparison of synthetic turbulence approaches for blade element momentum theory prediction of tidal turbine performance and loads. Renew. Energy 145, 408–418.

United Nations, 2015. The 17 sustainable development goals. URL: https://sdgs.un.org/goals. (Accessed 12 May 2025).